HHS Public Access

Author manuscript

Colloids Surf B Biointerfaces. Author manuscript; available in PMC 2019 July 30.

Published in final edited form as:

Colloids Surf B Biointerfaces. 2018 October 01; 170: 673–682. doi:10.1016/j.colsurfb.2018.06.050.

Colloidal stability as a determinant of nanoparticle behavior in the brain

Chad Curtis[a], **Dorsa Toghani**[b], **Ben Wong**[c], **Elizabeth Nance**[a,*]

[a]Department of Chemical Engineering, University of Washington, Seattle, WA, 98195, United States

[b]Department of Bioengineering, University of Washington, Seattle, WA, 98195, United States

[c]Math Academy, College of Engineering, University of Washington, Seattle, WA, 98195, United States

Abstract

Drug delivery to the brain is challenging due to a highly regulated blood-brain barrier (BBB) and a complex brain microenvironment. Nanoparticles, due to their tailorability, provide promising platforms to enhance therapeutic delivery and achieve controlled release and disease-specific localization in the brain. However, we have yet to fully understand the complex interactions between nanoparticles and the biological environments in which they operate. It is important to perform a systematic study to characterize nanoparticle behavior as a function of ion composition, concentration, and pH in cerebrospinal fluid (CSF). These could alter nanoparticle biological identity and influence diffusive capability and cellular uptake. In this study, poly(ethylene glycol) (PEG)-coated and carboxyl-coated polystyrene (PS-PEG and PS-COOH respectively) nanoparticles (NPs) were used to evaluate the aggregation kinetics, colloidal stability, and diffusive capability of nanoparticles in conditions relevant to the brain microenvironment. Size, surface charge, and surface coating were varied in a range of CSF ion concentrations and compositions, pH conditions, and temperatures. Small changes in calcium concentration and pH destabilize nanoparticles in CSF. However, PS-PEG NPs remain stable over a wider variety of conditions than PS-COOH NPs, and have higher diffusion capabilities in both agarose gels, an *in vitro* model of the brain microenvironment, and an organotypic brain tissue slice model. These results demonstrate the need for steric stabilization to maintain nanoparticle colloidal stability in a wide range of conditions. Importantly, colloidal stabilization allows for increased diffusive capability and can be used to predict diffusive behavior in the brain microenvironment.

Keywords

Diffusion; Colloidal stability; Nanoparticles; Brain disease; Drug delivery

*Corresponding author. eanance@uw.edu (E. Nance).

Appendix A. Supplementary data

Supplementary material related to this article can be found, in the online version, at doi:https://doi.org/10.1016/j.colsurfb.2018.06.050.

1. Introduction

Neurological disorders cost around $900 billion per year to treat and represent 11% of the global burden of disease [1]. Importantly, therapeutic delivery to the brain shows that 98% of small-molecule therapeutics and ~ 100% of large-molecule therapeutics are ineffective in reaching target sites in the brain [2]. Drug delivery to the brain is challenging, due in part to the strictly regulated blood-brain barrier (BBB) and blood cerebrospinal fluid (CSF) barrier, and the complex microenvironment in which therapeutics must navigate to reach target sites. Nanoparticles can provide a vehicle for delivering therapeutics to overcome these barriers [3,4]. Nanoparticle platforms have been successful in effectively delivering drugs to the brain due to tailored control over nanoparticle physicochemical properties, in particular nanoparticle size, surface charge, and surface functionality [5,6].

When administered systemically, a nanoparticle must remain stable in blood, overcome the BBB, and then navigate the extracellular space (ECS) to selectively act on or uptake in disease cells. Nanoparticle stability has been evaluated in serum [7], blood [8–10], and saline [11,12] as a function of size, surface charge, and surface functionality. Size and surface coating are also physicochemical factors that have been explored for nanoparticle uptake across the intact and impaired BBB [13–17], in addition to shape and particle rigidity [18,19]. By crossing the BBB, nanoparticles can provide cell-specific uptake, including targeted delivery to lysosomes within neurons [20], and selective targeting of microglia and astrocytes to suppress inflammation and oxidative stress [16,21,22]. However, once across the BBB, nanoparticles are exposed to a physical and chemical environment that is unique to the brain. Physically, nanoparticle size is a particularly important parameter for penetration within the brain ECS [6]. Pore sizes within the brain have been estimated to be anywhere from 30 to 65 nm [23] to 20–225 nm in width [17], based on the methods of probing the ECS. Yet, there is a significant decrease in the ability of a nanoparticle to move within the brain parenchyma at sizes larger than 100 nm, suggesting an upper limit on nanoparticle size for effective drug delivery to the brain [17]. Size has also been shown to influence nanoparticle compartmentalization in brain cells [24]. Additionally, surface charge and surface functionality, including relative hydrophobicity, can be predominant factors in determining a particle’s ability to effectively diffuse within the brain extracellular matrix [17,25,26].

Importantly, all prior measurements to assess the impact of physicochemical properties on brain uptake and penetration within the brain parenchyma assume particles remained stable (no agglomeration or aggregation) not just in blood while circulating, but also in the brain environment. Yet, there is little evidence demonstrating that nanoparticles remain stable in brain microenvironment conditions. Therefore, there is a need to perform characterization of nanoparticle size and stability as a function of ion composition, concentration, or pH in brain extracellular fluid, all factors in the brain microenvironment. For example, calcium is a unique factor in the brain due to its presence in free form and varies spatially and temporally based on local cellular activity [27,28]. Like calcium, pH levels vary spatially and temporally in the brain [29]. Changes in pH can alter the protonation state of functional groups on the nanoparticle surface, which can also change nanoparticle stability. Each of

these factors could alter a nanoparticle's biological identity in the brain ECS, which could influence diffusive capability and cellular uptake of a therapeutic platform [30].

This study sought to systematically characterize nanoparticle behavior in representative brain microenvironment conditions to determine the predictive ability of colloidal stability on diffusive capability. Poly(ethylene glycol) (PEG)-coated and carboxyl-modified polystyrene (PS-PEG and PS-COOH respectively) nanoparticles from 60-to 2000 nm were used to evaluate nanoparticle behavior in conditions present in the brain microenvironment. PEG sterically stabilizes nanoparticles, and provides stealth capabilities that reduce the interaction with the surrounding environment [31]. In the context of aggregation kinetics, the comparison of PS-COOH and PS-PEG particles is useful in demonstrating the differences between electrocratically and sterically-stabilized nanoparticles. Additionally, nanoparticles are normally characterized at room temperature in low concentration NaCl solutions or saline solutions [32], and higher temperatures at physiological conditions could destabilize nanoparticles. Sterically-stabilzied nanoparticles can be sensitive to changes in temperature of just 1–2 °C [33]. Therefore, this study evaluated the aggregation kinetics, colloidal stability, and diffusive capability of nanoparticles with varying size, surface charge, and surface coating in a range of brain interstitial fluid ion concentrations and compositions, pH conditions, and temperature.

2. Materials and methods

2.1. Nanoparticle preparation and characterization

60, 100, 200, 500, 1000 and 2000-nm fluorescent COOH-modified PS nanoparticles (Fisher Scientific, Hampton, NH) were covalently modified with methoxy (MeO)-PEG-amine (NH_2) (5 kDa MW, Creative PEG Works, Winston-Salem, NC) by carboxyl amine reaction [34]. Briefly, 50–100 μL of PS particle suspension was washed and resuspended to 2-to 6-fold dilution in ultrapure water. An excess of MeO-PEG-NH_2 was added to the particle suspension and mixed to dissolve the PEG. *N*-Hydroxysulfosuccinimide (MilliporeSigma, Burlington, MA) and 200 mM pH 8.2 borate buffer was added to a 4-fold dilution of the starting volume. 1-Ethyl-3-(3-dimethyla-minopropyl) carbodiimide (EDC, Invitrogen, Carlsbad, CA) was added to stoichiometrically complement the added MeO-PEG-NH_2. Particle suspensions were placed on a rotary incubator for 4 h at 25 °C and then centrifuged (Amicon Ultra 0.5 mL 100k MWCO; MilliporeSigma) at conditions specified by Nance et al. [34]. Particles were resuspended in ultrapure water to the initial particle volume and stored at 4 °C until use. The hydrodynamic diameter, polydispersity index (PDI), and ζ-potential were measured for COOH-and PEG-coated fluorescent nanoparticles of all sizes. Particles were diluted to ~ 0.002% solids in filtered (0.45 μm, Whatman, Maidstone, UK) 10 mM NaCl and incubated for 24 h prior to measurement. Additional characterization was performed in artificial cerebrospinal fluid (ACSF) without calcium chloride ($CaCl_2$) to assess properties in *in vitro.*

2.2. Media preparation

ACSF was prepared with the addition of the following concentrations of reagents to deionized (DI) water: 119 mM NaCl (MilliporeSigma), 26.2 mM $NaHCO_3$

(MilliporeSigma), 2.5 mM KCl (MilliporeSigma), 1 mM NaH_2PO_4 (MilliporeSigma), 1.3 mM $MgCl_2$ (MilliporeSigma), and 10 mM glucose (MilliporeSigma). The solution was filtered (0.45 μm) in a sterile environment and stored at 4 °C. For individual experiments, aliquots of ACSF were taken and $CaCl_2$ added, then the media was allowed to equilibrate at desired conditions (23 °C/37 °C and 5% CO_2) for 1 h and adjusted to the appropriate pH (5.5, 7.2, or 8.5) with 0.2 mM HCl or 1 N NaOH.

2.3. In vitro particle aggregation via dynamic light scattering

Stock 1 M $CaCl_2$ and $MgCl_2$ solutions were prepared in DI water, from which 0.5, 1.0, 2.0, 4.0, 5.0, 8.0, and 10.0 mM dilutions were made. PS-COOH and PS-PEG nanoparticles were diluted in these salt solutions to achieve a concentration of 0.002% solids. Nanoparticle suspensions were allowed to sit for 24 h before measuring their hydrodynamic diameters *via* dynamic light scattering (DLS) (NanoSizer Zeta Series, Malvern Instruments, Malvern, UK). Number means were reported for static studies as recommended by EU directive 2011/696/ EU [32]. Z-average diameters were reported for aggregation studies. While z-average values can be inaccurate for polydisperse samples, these measurements are less vulnerable to noise, and some inaccuracy is inevitable in high-time resolution measurements *via* DLS.

2.4. Aggregation kinetics via dynamic light scattering

Particle-free media was allowed to reach temperature (23 °C or 37 °C) in the Zetasizer followed by a three-minute equilibration period. Nanoparticles were quickly added and mixed to achieve a concentration of 0.002% solids, and hydrodynamic diameter measurements were then taken every 10 s for 50 measurements (total time: 8 min 20 s). The measurements were paused briefly in order to add enough 1 M $CaCl_2$ solution to achieve 0.5 mM $CaCl_2$, and another 50 measurements in 10 s intervals were taken. This process was repeated for successive $CaCl_2$ concentrations of 1, 2, 3, 4, 5, 6, 8, and 10 mM.

For pH measurements, ACSF without $CaCl_2$ was prepared as described above. Aliquots of ACSF were allowed to equilibrate at the desired conditions (23 °C and 5% CO_2) for 1 h and adjusted to pH 7.2, and $CaCl_2$ was added to achieve 3 mM concentration. Nanoparticles were added and mixed to achieve a concentration of 0.002% solids. Potentiometric titrations were performed to assess pH as a function of acid/base added (see Figure S1). Starting at pH 7.2, 0.2 M HCl or 1 N NaOH was added in 1–40 μL increments and the pH read until the pH reached either 3 or 11.

For kinetic studies as a function of pH, aliquots of ACSF were allowed to equilibrate at the desired conditions (23 °C and 5% CO_2) for 1h and adjusted to pH 7.2, and $CaCl_2$ was added to achieve 3mM concentration. Hydrodynamic diameters measurements were taken every 10 s for 50 measurements. The measurements were paused briefly in order to add enough acid to reach the nearest 0.5 pH unit neighbor (7.0 or 7.5) as calculated from the potentiometric curve above, and another 50 measurements in 10-second intervals were taken. Measurements were paused, acid/base added, and restarted at successive pHs (7.0, 6.5, 6.0, 5.5, 5.0, 4.5, 4.0, 3.5, and 3.0 for acid; 8.0, 8.5, 9.0, 9.5, 10.0, 10.5, and 11.0 for base).

2.5. Gel diffusion studies

0.4% agarose gels in ACSF ($CaCl_2$ concentrations of 0, 3, 5, and 10 mM, pH 7.2) were prepared by adding 40 mg agarose (low EEO, gel point for 1.5% gel, 36 ± 1.5 °C, MilliporeSigma) to ACSF. The agarose-ACSF mixture was heated to 99 °C and mixed well until the agarose was completely dissolved, as indicated by no visible particulates in the solution. 400 μL agarose-ACSF was added to a well in an 8-well imaging plate and PS-COOH or PS-PEG nanoparticles were quickly added and mixed until evenly distributed to achieve a concentration of 0.005% solids. Four samples were prepared per particle type-condition combination. The prepared gels were allowed to set overnight at room temperature. Prior to imaging, the gels were allowed to incubate at 37 °C and 5% CO_2 for 30 min.

Five videos were collected per well with four wells at 10 Hz and 40x magnification for 6.5 s *via* fluorescent microscopy using a cMOS camera (Hamamatsu Photonics, Bridgewater, NJ) mounted on a confocal microscope (Nikon Instruments, Melville, NY). Nanoparticle trajectories were calculated *via* MOSAIC multi-particle tracking ImageJ plugin (National Institutes of Health, Bethesda, MD, USA) [35], and geometrically averaged precision-weighted mean squared displacements (MSD) were calculated *via* a self-developed Python package (DOI 10.5281/zenodo.1214158).

For polydispersity-dependent studies, gels were prepared using the method described above in ACSF without calcium chloride with either equal weight percent (20%) or equal number percent (20%) samples of 100, 200, 500, 1000, and 2000 nm PS-COOH or PS-PEG NPs. Videos were collected and analyzed using the same parameters described above.

For time-dependent aggregation studies, gels were prepared using the method described above in ACSF with 5 mM calcium chloride, but gels were not allowed to set overnight. Gels set for three hours to ensure complete gelation, and videos were collected and analyzed at 0, 1, 4, and 24 h prior to the three-hour gelation period.

2.6. Diffusion studies in cerebral cortex of neonatal rats

For rat brain tissue slices, all experiments were carried out at University of Washington in accordance with National Institutes of Health guidelines and local Institutional Animal Care and Use Committee regulations. Brain slices were prepared from 30 to 40 g postnatal day 14 (P14) Sprague-Dawley rat pups [17,36]. Briefly, animals were administered an intravenous injection of pentobarbitol (150 mg/kg). After euthanasia, the brain was rapidly removed and immersed in cold dissecting media consisting of 500 mL HBSS (Fisher Scientific), 1% Penicillin-Streptomycin (MilliporeSigma), and 3.2 g glucose (MilliporeSigma). 300μm-thick coronal slices (n = 4 per rat) were prepared using a tissue chopper (Ted Pella, Redding, CA). The tissue chopper and razor blades were washed with 70% ethanol prior to sectioning. Slices were placed in a Petri dish containing dissecting media and separated under a surgical dissection microscope. Individual slices were placed on 30 mm cell culture inserts (Fisher Scientific) in 6-well plates (Eppendorf, Hamburg, Germany) filled with 1.5 mL slice culture media containing 200 mL MEM (Fisher Scientific), 100 mL HBSS, 100 mL horse serum

(Fisher Scientific), 4 mL Glutamax (Fisher Scientific), and 1% Penicillin-Streptomycin. Slices were allowed to incubate in sterile conditions at 37 °C and 5% CO_2 overnight.

Prior to imaging slices were transferred to imaging dishes and 50 μL of either 0.02% solids 60, 100, 200, or 1000 nm PS-COOH or PS-PEG nanoparticles were added to the surface of the slices. Slices were allowed to incubate with particles for 30–60 minutes. Five videos were collected in the cortex of each slice at 10 Hz and 40x magnification for 6.5 s *via* fluorescent microscopy using a cMOS camera (Hamamatsu Photonics, Bridgewater, NJ) mounted on a confocal microscope (Nikon Instruments, Melville, NY). Nanoparticle trajectories were calculated *via* MOSAIC multi-particle tracking ImageJ plugin (National Institutes of Health, Bethesda, MD, USA) [35], and geometrically averaged precision-weighted MSD were calculated *via* a self-developed Python package.

2.7. Statistical analysis

Statistical analysis was performed using the sample Student *t*-test using GraphPad Prism 7.01 (GraphPad Software Inc). Differences were defined as statistically significant at $p < 0.05$, and the Holm-Sidak method was used to correct for multiple comparisons [37].

3. Results and discussion

3.1. Nanoparticle characterization

PS-COOH nanoparticles were compared with PS-PEG nanoparticles due to the widespread use of PEGylation as a method to sterically stabilize nanoparticle formulations and shield them from macrophage uptake *in vivo* [38]. All physicochemical nanoparticle properties for PS-COOH and PS-PEG nanoparticles used in this study are reported in Table 1. As expected, electrophoretic measurements of PS-COOH nanoparticles gave a ζ-potential of −20 to — 70 mV, depending on the size of the nanoparticle. Upon PEGylation of PS nanoparticles, all nanoparticles had an increase in measured hydrodynamic diameter of ~ 10–20 nm in size (Table 1), which is expected given the molecular weight of the PEG chain used (5 kDa) [39]. The decrease in magnitude of ζ-potential for PS-PEG nanoparticles compared to PS-COOH nanoparticles indicates that conjugation of PEG to the nanoparticle surface was successful.

3.2. Nanoparticle stability as a function of calcium and magnesium concentration

100 nm PS-COOH and PS-PEG colloidal stability was evaluated *in vitro* in solutions of $CaCl_2$ and magnesium chloride ($MgCl_2$). In $CaCl_2$ solutions, PS-COOH nanoparticles remained stable up to 2 mM salt concentration, but form aggregates at concentrations higher than 4 mM (Fig. 1A). PS-PEG nanoparticles remained stable in a biologically relevant range of calcium concentrations spanning 0–10 mM. Similar behavior for both particle types was found in $MgCl_2$ solutions; PS-COOH nanoparticles remained stable in solutions up to 4 mM $MgCl_2$ and aggregated at concentrations of 5 mM and higher (Fig. 1B). PS-PEG particles remained stable in $MgCl_2$ concentrations at least up to 10 mM.

CSF equilibrates with interstitial fluid (ISF), the fluid filling the extracellular space within the brain, in the ventricles and perivascular spaces within the brain [40]. ISF is a complex

fluid with composition that varies regionally due to metabolic and signaling processes of cells [41], and is difficult to measure, but can be regarded as similar to that of CSF. Within ISF and CSF, calcium plays a vital regulatory role, and is a unique factor in the brain due to its presence in free form [27,28]. Calcium is a universal messenger among multiple cell types throughout the body and is particularly important in the brain. Calcium is involved in regulating neurotransmitter synthesis and release, neuronal excitability, and phosphorylation, as well as long-term processes including memory and neuroplasticity [42]. Calcium is present at 2 mM in CSF under normal neurological conditions, but in the presence of injury or disease, calcium can become dysregulated, resulting in higher concentrations [43–45]. Calcium dysregulation is linked to brain aging [46,47], has been implicated in toxicity in glial cell populations, neurodegeneration, neuroinflammation [48], and can be a factor in multiple diseases including Alzheimer's disease, Parkinson's disease, amyotrophic lateral sclerosis, Huntington's disease, and spinocerebellar ataxias [49]. The therapeutic implications for changes in calcium concentration in the presence of injury is of particular interest given previous findings that show calcium concentration can be a significant factor in nanoparticle aggregation [50].

In the context of nanotherapeutics, changes in calcium concentrations in both the ECS and cell cytoplasm can ultimately affect drug efficacy. Increasing calcium concentrations reduces the electrostatic double layer (EDL) repulsive energy between particles. Once a critical concentration is reached, nanoparticle aggregation is initiated. The variation between calcium and magnesium threshold concentrations that cause PS-COOH nanoparticles to aggregate can be explained in terms of the different hydration behavior of calcium and magnesium ions. Magnesium ions have more tightly held water molecules due in part to their smaller size [51]. Water molecules are less likely to dissociate from magnesium ions than calcium ions, preventing them from binding to the negatively charged PS-COOH nanoparticles [52]. Both calcium and magnesium independently impact nanoparticle stability; however, both are simultaneously present in CSF. To determine the combined effects of these ions at different concentrations, additional experiments were performed in 1:1 M solutions of salts, *e.g.* magnesium sulfate ($MgSO_4$) and calcium chloride ($CaCl_2$). Nanoparticles in these mixtures exhibited behavior intermediate to the observed behavior in solutions of the separate component salts (Figure S2). For example, PS-COOH nanoparticles that form aggregates in $MgCl_2$ concentrations greater than 5 mM only begin to aggregate in 1:1 $MgCl_2$: $MgSO_4$ solutions at concentrations greater than 8 mM.

These studies raise additional questions regarding the relevance of particle size as a significant factor in nanoparticle aggregation, and the role the cation-associated anion associated has on nanoparticle aggregation. A similar static aggregation study using 60 nm PS-COOH and PS-PEG nanoparticles showed little difference in behavior from the 100 nm nanoparticles (Figure S3 A). 60 nm PS-COOH and PS-PEG nanoparticles tested in $MgSO_4$ also showed that, while the PS-COOH nanoparticles begin to aggregate at higher salt concentrations, the same rate of aggregation was not seen when compared with $MgCl_2$ (Figure S3B). This indicates that the anion also plays a role in determining nanoparticle stability [53], but the result was unexpected as it contradicts predictions made with the Hofmeister series [54]. In switching from chloride to sulfate, both the identity and the valence of the anion are varied. Polyvalent ions of either sign have a possibility of binding to

the nanoparticle surface. Measured ζ-potentials in 2 mM solutions of $MgCl_2$ and $MgSO_4$ indicate a more negative charge on 100 nm PS-COOH nanoparticles in $MgSO_4$ (−19.0 ± 0.7 and −21.0 ± 0.5 respectively, $p = 0.08$). The added negative charge could provide additional electrostatic stability.

3.3. Calcium-dependent aggregation of nanoparticles at multiple temperatures and pHs in ACSF

In acidic conditions (pH 5.5) and at room temperature (23 °C), 100 nm PS-COOH nanoparticles experienced aggregation effects at all $CaCl_2$ concentrations in ACSF (Fig. 2A). PS-COOH nanoparticles had a nominal size of 141.1 nm, which increased to 150.0 nm when $CaCl_2$ was increased to 0.5 mM after 10 min. This continued to increase in size at a rate of 4.2 ± 0.6nm/min until 8mM $CaCl_2$, when aggregation accelerated to 11.3 ± 1.8 nm/min. In these same conditions, 100 nm PS-PEG nanoparticles saw no significant increase in size (from 0.0 ± 0.2 nm/min to −0.4 ± 0.2 nm/min) and stayed constant over the entire range of $CaCl_2$ concentrations.

When the temperature was raised to body temperature (37 °C), the aggregation profiles changed. The baseline size at 0 mM $CaCl_2$ was 20 nm higher (160.6 nm) for 100 nm PS-COOH nanoparticles, but increased linearly, similar to the 23 °C profile. There was a similar acceleration to aggregation at the 8 mM threshold. 100 nm PS-PEG nanoparticles experienced an overall increase of 20 nm, indicating the potential onset of aggregation, and could result in large aggregates at long timescales. When temperature is increased, there are two effects at play that can alter stability: first, the PEG brush layer contracts; second, the hydrodynamic radii of the nanoparticles decrease. However, the compressed PEG layers also reduce the steric hindrance that sterically stabilizes nanoparticles. At high enough calcium concentrations, the PS-PEG nanoparticles also begin to aggregate.

Increasing the pH to 7.2 led to a change in behavior for both particle types (Fig. 2B). PS-COOH nanoparticles experienced significant aggregation at a threshold of 4 mM $CaCl_2$ at 25 °C (280.1 nm compared to 161.1 nm at 0mM $CaCl_2$, $p > 0.001$). After 6 mM $CaCl_2$, particles continued to increase in size overall, but experience downward trends after the initial addition of $CaCl_2$ to the solution. When increased to body temperature, PS-COOH nanoparticles aggregated at a threshold of 2 mM $CaCl_2$, continuing to increase in overall size, but then decrease following $CaCl_2$ addition similar to the 23 °C profiles. This indicates that larger aggregates > 1000 nm are settling out of solution. 100 nm PS-PEG nanoparticles remained stable at 23 °C, up until 6 mM where aggregation begins to occur. At 37 °C, PS-PEG nanoparticles remained stable until 1 mM $CaCl_2$ with modest increases in sizes until 3 mM $CaCl_2$. Above 3 mM, PS-PEG nanoparticles began to aggregate more rapidly, reaching sizes in excess of 1000 nm at 8mM $CaCl_2$ concentrations.

In basic conditions (pH 8.5), 100 nm PS-COOH nanoparticles had a very small range of stable $CaCl_2$ concentrations (Fig. 2C). At room temperature, PS-COOH nanoparticles remained stable up until 1 mM $CaCl_2$, but at body temperature, the addition of any $CaCl_2$ initiated aggregation. High pH causes protons to dissociate from carboxyl groups on the PS-COOH nanoparticles, generating a negative charge on the particle surface. The presence of divalent cations induces bridging effects between the PS-COOH nanoparticles, which is

accelerated at higher $CaCl_2$ concentrations. 100 nm PS-PEG nanoparticles are stable over a wider range of $CaCl_2$ concentrations than PS-COOH nanoparticles in basic conditions, and aggregate sizes are four-fold times smaller: PS-COOH nanoparticles reach ~4000nm at 10 mM $CaCl_2$, while PS-PEG nanoparticles reach ~ 1000 nm in similar conditions. The aggregation of PS-PEG nanoparticles is also likely due to bridging effects in the presence of calcium. The more negative charges of PS-PEG nanoparticles brought about by basic conditions can interact with calcium ions, and initiate aggregation events.

There was a demonstrated difference in colloidal stability of 100 nm PS-COOH and PS-PEG nanoparticles in ACSF at 2 mM $CaCl_2$ and pH 7.2. PS-PEG nanoparticles experienced little to no aggregation, while PS-COOH nanoparticles had a steep aggregation profile. This has important implications. First, the observed difference in diffusive ability in living brain tissue in previously published studies using PS-PEG and PS-COOH nanoparticles [17] could be in part due to the differences in nanoparticle colloidal stability. This study has shown that PS-COOH nanoparticles are colloidally unstable in ACSF at conditions similar to those in the brain, and small perturbations can worsen aggregation effects. Second, this study has demonstrated the importance of accounting for temperature when characterizing nanoparticles *in vitro*. PS-COOH nanoparticles aggregated in 2 mM $CaCl_2$ ACSF at body temperature (37 °C), but did not experience significant aggregation at room temperature (137.1 nm compared to 135.7 nm at 0mM $CaCl_2$, $p = 0.31$). PS-PEG nanoparticles also became destabilized at higher temperatures, but to a lesser extent. Temperature can affect nanoparticle stability by changing dissociation rates for electrostatically stabilized colloids and by structural changes for sterically stabilized colloids [55], and therefore should be accounted for when performing *in vitro* characterization of nanoparticles for *in vivo* applications.

3.4 pH-dependent aggregation of nanoparticles in ACSF

To explore the effect of pH on nanoparticle aggregation, pH was adjusted by 0.5 pH units every ten minutes. In increasingly acidic conditions in ACSF, 100 nm PS-COOH nanoparticles remained stable up to pH 6.5, where aggregation began (Fig. 3A). Particle sizes plateaued at 2000 nm at pH 5.0 and did not increase further with more acidic pH conditions. 100 nm PS-PEG nanoparticles remained stable at all acidic pH conditions in ACSF. In increasing basic conditions, PS-COOH nanoparticles began aggregating at pH 7.5 and continued to increase in size beyond a hydrodynamic diameter of 10 μm (Fig. 3B). PS-PEG nanoparticles began to aggregate at pH 8.0, reaching maximum sizes of 6 μm at pH 11.

PS-COOH nanoparticles had a narrow range of stability in ACSF (7.0–7.5), while PS-PEG nanoparticles had a much wider range, especially in acidic conditions (3.0–8.0). PEGylated nanoparticles are stabilized through a steric mechanism, while the PS-COOH nanoparticles are electrocratically stabilized and are more sensitive to changes in the ionic environment. In the presence of divalent cations and a relatively high ionic strength (~160mM compared to 10 mM in standard characterization techniques), the magnitude of the ζ-potential of PS-COOH nanoparticles is small compared to characterization measurements in 10 mM NaCl (Figure S4). With little electrostatic repulsion present, PS-COOH nanoparticles are unstable in ACSF and can aggregate readily in response to small fluctuations in pH and divalent

cation concentration. In basic conditions, the surface charge of PS-COOH nanoparticles become more negative as the carboxyl groups become deprotonated. This leads to an increase in bridging effects due to the presence of calcium, resulting in high instability in basic conditions. As pH becomes more acidic, the surface charge becomes less negative, eventually passing the point of zero charge (~pH 6.5) and triggering the onset of aggregation [56]. However, particle size does not continue to increase as pH becomes more acidic, as the low pH results in positively charged particles and the restoration of electrostatic repulsion.

Although sterically-stabilized, PS-PEG nanoparticles can still be susceptible to aggregation effects as a function of pH. As pH becomes more basic, PS-PEG nanoparticles do begin to aggregate at ~pH 8. This could be due to interactions with calcium ions at unreacted carboxyl sites on the nanoparticle surface. The PS-PEG nanoparticles have a slight negative charge in pH 7 ACSF and are more negative as pH becomes more basic (Figure S5). At more basic pH, these interactions are strong enough to cause bridging between calcium ions and PS-PEG nanoparticles. As pH shifts towards more acidic, PS-PEG nanoparticles do not aggregate, even as ζ-potentials become near-neutral, indicating that the steric stability lent by the PEG layer prevents any aggregation events from occurring.

3.5. Impact of calcium concentration on nanoparticle diffusion in gel model

To assess the impact of colloidal stability on nanoparticle diffusion, 100 nm PS-COOH and PS-PEG nanoparticles were tracked using highspeed multi-particle tracking (MPT) [17,57] in an agarose gel, a representative geometric model of the brain microenvironment [58]. Diffusion coefficients for both 100 nm PS-COOH and PS-PEG nanoparticles depend on calcium concentration in the gel (Fig. 4A, B). Representative frames from MPT videos are in Figure S6. Diffusion coefficients of PS-COOH nanoparticles decrease as calcium concentration is increased (Fig. 4C). At calcium concentrations exceeding 5 mM, PS-COOH nanoparticles become immobilized. As shown previously in Fig. 2, 100 nm PS-COOH nanoparticles begin aggregating at calcium concentrations of 2 mM. Thus, the immobility in gels is likely due to both bridging effects between nanoparticles resulting in aggregation and bridging effects with agarose molecules resulting in tethering. At 10 mM calcium chloride, 100 nm PS-COOH nanoparticles are immobilized even further (diffusion coefficient 95% CI: 1.69×10^{-3}–1.71×10^{-3} $\mu m^2/s$)

PS-PEG nanoparticles also exhibit changes in diffusive behavior as calcium concentration is modified. In general, 100 nm PS-PEG diffusion coefficients decrease as calcium concentration is increased (Fig. 4C). However, in all cases, the particles remain mobile, with diffusion coefficients of similar magnitude across the entire range of calcium concentration tested. As shown in Fig. 2, the steric stability of PS-PEG nanoparticles improves their aggregation profiles in ACSF, but the particles do begin to aggregate at calcium concentrations higher than 2 mM in ACSF at pH 7.2 and 37 °C. This reduction in aggregation can allow PS-PEG nanoparticles to retain their diffusive ability over a wider range of calcium concentrations than PS-COOH nanoparticles.

Both size exclusion due to large particle aggregates and deposition in the gel could contribute to the reduced diffusive behavior of 100 nm PS-COOH NPs. To verify the impact of size exclusion on observed diffusion coefficients, and decouple the effects of size

exclusion and altered nanoparticle-agarose interactions due to increased calcium levels, we performed multi-particle tracking experiments of various mixtures of PS-COOH and PS-PEG nanoparticles in ACSF without calcium chloride (non-aggregating conditions) to mimic aggregating nanoparticle at various stages of aggregation. We used an equal weight percent mixture of 100, 200, 500, 1000, and 2000 nm nanoparticles to represent early stage aggregation; an equal number percent mixture of 100, 200, 500, 1000, and 2000 nm nanoparticles to represent a later stage of aggregation; and 2000 nm nanoparticles to represent a long-term stage of aggregation. The physicochemical properties of the constituent particles are shown in Table 1.

Larger particles will have reduced MSDs due solely to reduced Brownian motion as predicted by Stokes-Einstein, but pore size restrictions will prevent large particles from diffusing at all. This effect can be observed in Fig. 5. The equal-weight particle mixture is unhindered when compared with the 100 nm PS-COOH NPs in similar conditions (Fig. 5A, diffusion coefficient 95% CI 4.799×10^{-1}–4.803×10^{-1} $\mu m^2/s$ compared to 3.555×10^{-1}–3.557×10^{-1} $\mu m^2/s$). The small number of larger particles mimicking early-stage aggregates do not affect the average behavior. The equal-number particle mixture has reduced diffusive behavior, due to a higher concentration of immobilized particles (Fig. 5B, diffusion coefficient 95% CI: 1.389×10^{-2}–1.394×10^{-2} $\mu m^2/s$). It is only in the 2000 nm case the MSD profile essentially flatlines (Fig. 5C, diffusion coefficient 95% CI: 1.550×10^{-3}–1.555×10^{-3} $\mu m^2/s$). Particle sizes smaller than the average pore size are a necessary but not sufficient condition for effective diffusive ability in porous media. For both PS-COOH and PS-PEG nanoparticles, the diffusive behavior decreases as the average particle size increases. In all cases, PS-COOH and PS-PEG profiles are similar (with more discrepancy in the equal number case) with PS-PEG profiles being less than the PS-COOH profiles (2000 nm PS-PEG diffusion coefficient 95% CI: 9.11×10^{-4}–9.15×10^{-4} $\mu m^2/s$). This can be partly attributed to the reduced diffusion coefficients predicted by Stokes-Einstein due to the larger size of the PS-PEG NPs.

While polydisperse samples can be introduced into the gel model, it is more difficult to systematically probe the effect of polydispersity. Ideally, one would have a set of nanoparticles with similar average particle sizes and varying polydispersity. We do not provide a systematic evaluation of polydispersity here. It is known that particles of different sizes have different deposition rates and filtration coefficients in porous media as demonstrated in an analytical model by Yang et al. [59]. Yoon et al. examined the effect of polydispersity on particle transport properties experimentally using a polydisperse sample of 1–25 μm fluorescent particles in a medium of monosize 4 mm glass beads [60]. They demonstrate that for polydisperse samples, transport properties vary with depth in the porous medium due to filtration of larger particles near the inlet. As our particles were pre-mixed prior to gelation, there should be no variation of diffusive properties as a function of depth.

An additional level of complexity introduced into a model of aggregating particles in porous media is the effect of time dependence. Both average size and polydispersity are changing with time, as shown in Fig. 2. If the time scale of aggregation and the time scale of measurement are similar, this could make any resulting diffusion data unreliable. In order to evaluate the impact of absolute time on the collected MSD data, we collected videos in gels

of aggregating 100 nm PS-COOH and PS-PEG nanoparticles at 0, 1, 4, and 24 h after the gels had set. The results are shown in Fig. 6. The measured diffusion coefficients of the PS-COOH nanoparticles decrease over time (diffusion coefficient CIs: 3.788×10^{-1}–3.789×10^{-1}, 2.978×10^{-1}–2.979×10^{-1}, 2.036×10^{-1}–2.037×10^{-1}, 4.169×10^{-2}–4.172×10^{-2} $\mu m^2/s$ at 0, 1, 4, and 24 h). This can be attributed to the greater proportion of large aggregates at later timepoints. The PS-PEG diffusion coefficients are more stable over time (diffusion coefficient CIs: 5.269×10^{-1}–5.270×10^{-1}, 4.113×10^{-1}–4.113×10^{-1}, 3.850×10^{-1}–3.851×10^{-1}, 3.856×10^{-1}–3.857×10^{-1} $\mu m^2/s$ at 0, 1, 4, and 24 h), which can also be attributed to their shallower aggregation profiles as shown in Fig. 2. In order to minimize the effect of absolute time as a factor in our gel model, we collected all data in gels after a 24 h gelation period. This ensures that the gel is fully set and that aggregation is not present during video collection.

In order to determine whether a nanoparticle's diffusive ability could be predicted by its aggregation behavior in an *in vitro* environment, the nanoparticle diffusion coefficients were plotted against the hydrodynamic diameters as measured by DLS in ACSF as a function of calcium concentration (Fig. 7). There is a precipitous drop in diffusive ability in agarose gels when particle aggregates reach sizes between 1200 and 1600 nm. When nanoparticle sizes are less than 1200 nm, the diffusion coefficients in gels are of the same magnitude independent of the mechanism of stabilization (steric *vs* electrostatic). However, nanoparticle diffusive behavior cannot entirely be explained by aggregation state. Even with similar hydrodynamic diameters (150–160 nm), PS-COOH nanoparticles have roughly half the diffusion coefficient of PS-PEG nanoparticles. Instead, the division of nanoparticle behavior into two diffusive regimes demonstrates that the diffusive ability on nanoparticles in a gel model of the brain can be predicted based on its hydrodynamic diameter as measured by DLS. This could potentially be translated into a screening tool before nanoparticles are used in *ex vivo* and *in vivo* experiments.

Interestingly, PS-COOH nanoparticles retained their diffusive behavior in up to 3 mM $CaCl_2$ in ACSF in agarose gels. PS-COOH retention of diffusive ability did not seem to coincide with the observed aggregate size of > 1000 nm in ACSF at the same conditions. These results are indicative of potential limitations of the agarose gel model. A gel model of the brain should account for both macro-and micro-scale rheology, with a distribution of effective pore spacing within the gel that are representative of the distribution of extracellular spaces in the brain parenchyma. Pore sizes in agarose gels scale with agarose concentration according to the power law $a \sim C^{-\gamma}$ [61]. Using the model proposed by Pernodet et al. and confirmed *via* atomic force microscopy measurements, this estimates a pore size of approximately 1000 nm for 0.4% agarose gels. Other experiments using positive pressure infusion have estimated pore sizes in low-concentration agarose gels to be between 10–100 nm [58], on which the present experiments were based. The presence of larger pores on the order of ~ 1000 nm could explain why even in the presence of aggregation, PS-COOH nanoparticles are able to diffuse in agarose gels, whereas in living brain diffusion, PS-COOH nanoparticle diffusion is limited [17].

3.6. Impact of calcium concentration on nanoparticle diffusion in a brain tissue model

In order to test whether aggregate size as measured *via* DLS in ACSF can be used to predict diffusive behavior in the brain, we also performed diffusion experiments in an organotypic slice model of the brain in P14 Sprague-Dawley rats. Two particle types (PS-COOH and PS-PEG) and four base particle sizes (60, 100, 200, and 1000 nm) were used. Results are shown in Fig. 8. PS-COOH MSD profiles decreased as a function of base particle size (diffusion coefficient CIs 2.960×10^{-2}–2.962×10^{-2}, 1.656×10^{-2}–1.662×10^{-2}, 1.274×10^{-2}–1.280×10^{-2}, 7.36×10^{-4}–8.80×10^{-4} $\mu m^2/s$ for 60, 100, 200, and 1000 nm nanoparticles, respectively). PS-PEG MSD profiles similarly decreased with increasing size (diffusion coefficient CIs 1.2952–1.2954, 2.078×10^{-1}–2.081×10^{-1}, 1.0596×10^{-1}–1.0602×10^{-1}, 1.45×10^{-2}–1.51×10^{-2} $\mu m^2/s$ for 60, 100, 200, and 1000 nm nanoparticles, respectively). In all cases, PS-PEG nanoparticles had higher diffusion coefficients than their size-equivalent PS-COOH counterparts.

Similar to the results in the gel model, it is difficult to parse out all the contributors to the reduced diffusion coefficients of PS-COOH nanoparticles when compared with PS-PEG nanoparticles. Both particle-particle interactions (resulting in aggregation) and particle-microenvironment interactions (resulting in deposition) play a role. In order to determine if differences in diffusive behavior can be accounted for by altered aggregation states when particles are administered to tissue, while ignoring many of the particle-environment factors, we plotted the hydrodynamic diameters of PS-COOH and PS-PEG nanoparticles as measured in ACSF (Table S1) against the measured diffusion coefficients at 1 s (Fig. 9). PS-COOH nanoparticles have increased size in ACSF, indicative of aggregation, as shown in previous data in this paper. There is a linear relationship between the log diffusion coefficient measured in tissue and the log hydrodynamic diameter measured in ACSF (R^2 = 0.85). This suggests that the magnitude of the diffusive ability of nanoparticle formulation can be predicted with DLS measurements, particularly for aggregating nanoparticles.

We noted that the thresholding phenomenon observed in the gel model was not replicated in the organotypic brain tissue model. Particles in tissue exhibit a more gradual decrease in diffusion coefficients as a function of hydrodynamic diameter when compared to the gel model. However, the same general decreasing trend in diffusion with increasing nanoparticle size is observed. Also, if we apply the threshold value suggested from the gel model (1600 nm), all particles that had hydrodynamic diameters below the indicated threshold had diffusion coefficients greater than $1.0 \times 10^{-2} \mu m^2/s$.

The methods used in this paper include both *in vitro* and *ex vivo* techniques, which allows for fine-tuned control of parameters of interest and inclusion of complex biological environments. However, this approach does not account for other factors present in the brain microenvironment, including spatial and temporal changes brought about by normal function (e.g. respiration, sleep), ongoing injury, or development, the presence of proteins in the ECS, and regional differences in brain structure and function. Each of these additional functionalities can be incorporated into gels as advancements in biomaterials continues to grow [62–66]. Future studies can examine the competing kinetics of nanoparticle transport with aggregation effects. In the brain microenvironment, aggregation occurs simultaneously with particle transport through the tissue. A theoretical model of nanoparticle diffusion in

porous media with simultaneous aggregation could explore the effects of pore size, nanoparticle size, and rate of aggregation on nanoparticle diffusion. Previous studies have examined the effect of aggregate size on cellular uptake and toxicity [67], but little is known about how aggregation effects change as nanoparticles partition or permeate across a boundary and through a tissue environment. Future *ex* vivo and *in vivo* experiments could look at the effect of cellular uptake, intracellular and intra-organelle aggregation.

4. Conclusion

Characterization of nanoparticles in standard media, as well as in biological milieu at physiologically relevant conditions, can reduce the number of ex vivo and *in vivo* tests that are necessary to evaluate nanoparticle behavior in vivo. Importantly, systematic characterization of colloidal stability can be extended to pathological conditions, which can have implications for nanoparticle behavior in diseased states. For example, it is known that calcium regulation in the brain ECS is altered in neuroinflammation, neurodegeneration [48], and brain aging [42], all of which could affect nanoparticle aggregation kinetics. In addition, nanoparticles have also been used for intracellular targeting, including mitochondria, lysosomes, and the nucleus [68]. Factors such as calcium and pH are highly variable in these intracellular compartments due to cellular control mechanisms [69,70], indicating that stability should be assessed based on the relevant target conditions for the nanoparticle. Colloidal stability of nanoparticle formulations in physiologically relevant media can significantly affect the diffusive behavior of nanoparticles in the brain microenvironment, and by extension, delivery of therapeutic payloads to targets of interest in the brain.

Supplementary Material

Refer to Web version on PubMed Central for supplementary material.

Acknowledgements

This publication was supported by the National Institute of General Medical Sciences MIRA1R35GM124677-01 and the National Center for Advancing Translational Sciences of the National Institutes of Health under Award Number TL TR002318 (C. Curtis). This work was facilitated though the use of advanced computational, storage, and networking infrastructure provided by the Hyak supercomputer system at the University of Washington. The authors would like to thank Prof. John Berg for his critiques and insights in final drafting of this manuscript. The authors would also like to thank M. McKenna for his edits and suggestions in final drafting of this manuscript. The content is solely the responsibility of the authors and does not necessarily represent the official views of the National Institutes of Health.

References

[1]. DALYs GBD and Collaborators H, 2017 Global, regional, and national disability-adjusted life-years (DALYs) for 333 diseases and injuries and healthy life expectancy (HALE) for 195 countries and territories, 1990–2016: a systematic analysis for the Global Burden of Disease Study 2016. Lancet, 390(10100): p. 1260–1344. [PubMed: 28919118]

[2]. Pardridge WM, The blood-brain barrier: bottleneck in brain drug development, NeuroRx 2(1) (2005) 3–14. [PubMed: 15717053]

[3]. Mayberg M, et al., Perivascular meningeal projections from cat trigeminal ganglia: possible pathway for vascular headaches in man, Science 213(4504) (1981) 228–230. [PubMed: 6166046]

[4]. Zhou Y, et al., Crossing the blood-brain barrier with nanoparticles, J. Control Release 270 (2018) 290–303. [PubMed: 29269142]

[5]. Comoglu T, Arisoy S, Akkus ZB, Nanocarriers for effective brain drug delivery, Curr. Top. Med. Chem. 17(13) (2017) 1490–1506. [PubMed: 28017157]

[6]. Curtis C, et al., Systems-level thinking for nanoparticle-mediated therapeutic delivery to neurological diseases, Wiley Interdiscip. Rev. Nanomed. Nanobiotechnol. (2016).

[7]. Rausch K, et al., Evaluation of nanoparticle aggregation in human blood serum, Biomacromolecules 11 (11) (2010) 2836–2839. [PubMed: 20961117]

[8]. Lacerda SHD, et al., Interaction of Gold nanoparticles with Common human blood proteins, Acs Nano 4 (1) (2010) 365–379. [PubMed: 20020753]

[9]. Tenzer S, et al., Rapid formation of plasma protein corona critically affects nanoparticle pathophysiology, Nat. Nanotechnol. 8(10) (2013) 772–U1000. [PubMed: 24056901]

[10]. Fornaguera C, et al., Interactions of PLGA nanoparticles with blood components: protein adsorption, coagulation, activation of the complement system and hemolysis studies, Nanoscale 7(14) (2015) 6045–6058. [PubMed: 25766431]

[11]. French RA, et al., Influence of ionic strength, pH, and cation valence on aggregation kinetics of titanium dioxide nanoparticles, Environ. Sci. Technol. 43(5) (2009) 1354–1359. [PubMed: 19350903]

[12]. Chen KL, Mylon SE, Elimelech M, Enhanced aggregation of alginate-coated iron oxide (hematite) nanoparticles in the presence of calcium, strontium, and barium cations, Langmuir 23(11) (2007) 5920–5928. [PubMed: 17469860]

[13]. Zensi A, et al., Albumin nanoparticles targeted with apo E enter the CNS by transcytosis and are delivered to neurones, J. Controlled Release 137(1) (2009) 78–86.

[14]. Zensi A, et al., Human serum albumin nanoparticles modified with apolipoprotein a-I cross the blood-brain barrier and enter the rodent brain, J. Drug Target. 18(10) (2010) 842–848. [PubMed: 20849354]

[15]. Gulyaev AE, et al., Significant transport of doxorubicin into the brain with poly-sorbate 80-coated nanoparticles, Pharm. Res. 16(10) (1999) 1564–1569. [PubMed: 10554098]

[16]. Zhang F, et al., Surface functionality affects the biodistribution and microglia-targeting of intra-amniotically delivered dendrimers, J. Controlled Release 237 (2016) 61–70.

[17]. Nance EA, et al., A dense poly(ethylene glycol) coating improves penetration of large polymeric nanoparticles within brain tissue, Sci. Transl. Med. 4(149) (2012) 149ra119.

[18]. Kolhar P, et al., Using shape effects to target antibody-coated nanoparticles to lung and brain endothelium, Proc. Natl. Acad. Sci. U. S. A. 110(26) (2013) 10753–10758. [PubMed: 23754411]

[19]. Anselmo AC, et al., Elasticity of nanopartides influences their blood circulation, phagocytosis, endocytosis, and targeting, Acs Nano 9(3) (2015) 3169–3177. [PubMed: 25715979]

[20]. Bourdenx M, et al., Nanoparticles restore lysosomal acidification defects: implications for parkinson and other lysosomal-related diseases, Autophagy 12(3) (2016) 472–483. [PubMed: 26761717]

[21]. Sharma R, et al., Activated microglia targeting dendrimer-minocycline conjugate as therapeutics for neuroinflammation, Bioconjugate Chem. 28(11) (2017) 2874–2886.

[22]. Nance E, et al., Dendrimer-mediated delivery of N-acetyl cysteine to microglia in a mouse model of rett syndrome, J. Neuroinflammation 14 (2017).

[23]. Thorne RG, Nicholson C, In vivo diffusion analysis with quantum dots and dextrans predicts the width of brain extracellular space, Proc. Natl. Acad. Sci. U. S. A. 103(14) (2006) 5567–5572. [PubMed: 16567637]

[24]. Chaturbedy P, et al., Shape-directed compartmentalized delivery of a nanoparticle-conjugated small-molecule activator of an epigenetic enzyme in the brain, J. Controlled Release 217 (2015) 151–159.

[25]. Walters R, et al., The role of negative charge in the delivery of quantum dots to neurons, Asn Neuro 7(4) (2015).

[26]. Kreuter J, et al., Influence of the type of surfactant on the analgesic effects induced by the peptide dalargin after its delivery across the blood-brain barrier using surfactant-coated nanoparticles, J. Controlled Release 49(1) (1997) 81–87.

[27]. Siesjo BK, Calcium in the brain under physiological and pathological conditions, Eur. Neurol. 30 (1990) 3–9.

[28]. Berridge MJ, Neuronal calcium signaling, Neuron 21(1) (1998) 13–26. [PubMed: 9697848]

[29]. Wood JH, Neurobiology of Cerebrospinal Fluid vol. 1–2, Plenum Press, New York, 1980.

[30]. Monopoli MP, et al., Biomolecular coronas provide the biological identity of nanosized materials, Nat Nanotechnol 7 (12) (2012) 779–786. [PubMed: 23212421]

[31]. Immordino ML, Dosio F, Cattel L, Stealth liposomes: review of the basic science, rationale, and clinical applications, existing and potential, Int. J. Nanomed. 1(3) (2006) 297–315.

[32]. Bhattacharjee S, DLS and zeta potential -what they are and what they are not? J. Controlled Release 235 (2016) 337–351.

[33]. Napper DH, Steric stabilization J Colloid Interface Sci. 58 (2) (1977) 390–407.

[34]. Nance E, brain-penetrating nanoparticles for analysis of the brain microenvironment, Methods Mol. Biol. 1570 (2017) 91–104. [PubMed: 28238131]

[35]. Sbalzarini IF, Koumoutsakos P, Feature point tracking and trajectory analysis for video imaging in cell biology, J. Struct. Biol. 151 (2) (2005) 182–195. [PubMed: 16043363]

[36]. Zhang F, et al., Microglial migration and interactions with dendrimer nanoparticles are altered in the presence of neuroinflammation, J. Neuroinflammation 13(1) (2016) 65. [PubMed: 27004516]

[37]. Seaman MA, Levin JR, Serlin RC, New developments in pairwise multiple comparisons -some powerful and practicable Procedures, Psychol. Bull. 110 (3) (1991) 577–586.

[38]. Harris JM, Chess RB, Effect of pegylation on pharmaceuticals, Nat. Rev. Drug. Discov 2 (3) (2003) 214–221. [PubMed: 12612647]

[39]. Maisel K, et al., Nanoparticles coated with high molecular weight PEG penetrate mucus and provide uniform vaginal and colorectal distribution in vivo, Nanomedicine (Lond) 11 (11) (2016) 1337–1343. [PubMed: 27171816]

[40]. Milhorat TH, The third circulation revisited, J Neurosurg 42 (6) (1975) 628–645. [PubMed: 167134]

[41]. Abbott NJ, Bradbury MWB, Physiology and pharmacology of the blood-brain barrier, Handbook of Experimental Pharmacology, Springer-Verlag, Berlin; New York, 1992 xxiii, 549 p..

[42]. Gareri P, et al., Role of calcium in brain aging, Gen. Pharmacol. 26 (8) (1995) 1651–1657. [PubMed: 8745152]

[43]. Bito LZ, Davson H, Local variations in cerebrospinal fluid composition and its relationship to composition of extracellular fluid of cortex, Exp. Neurol. 14(3) (1966) p. 264–&. [PubMed: 4951842]

[44]. Thibault O, Gant JC, Landfield PW, Expansion of the calcium hypothesis of brain aging and alzheimer's disease: minding the store, Aging Cell. 6(3) (2007) 307–317. [PubMed: 17465978]

[45]. Nilsson P, et al., Calcium movements in traumatic brain injury: the role of glutamate receptor-operated ion channels, J. Cerebr. Blood F Met 16(2) (1996) 262–270.

[46]. Michaelis ML, Foster CT, Jayawickreme C, Regulation of calcium levels in brain tissue from adult and aged rats, Mech. Ageing Dev. 62(3) (1992) 291–306. [PubMed: 1583914]

[47]. Nicholson C, Interaction between diffusion and michaelis-menten uptake of dopamine after iontophoresis in striatum, Biophys. J. 68(5) (1995) 1699–1715. [PubMed: 7612814]

[48]. Fairless R, Williams SK, Diem R, Dysfunction of neuronal calcium signalling in neuroinflammation and neurodegeneration, Cell. Tissue Res. 357 (2) (2014) 455–462. [PubMed: 24326615]

[49]. Bezprozvanny IB, Calcium signaling and neurodegeneration, Acta Naturae 2 (1) (2010) 72–82.

[50]. Zhang Y, et al., Impact of natural organic matter and divalent cations on the stability of aqueous nanoparticles, Water Res. 43 (17) (2009) 4249–4257. [PubMed: 19577783]

[51]. Pavlov M, Siegbahn PEM, Sandstrom M, Hydration of beryllium, magnesium, calcium, and zinc ions using density functional theory, J. Phys. Chem. A 102(1) (1998) 219–228.

[52]. Deerfield DW 2nd et al., The role of hydrated divalent metal ions in the bridging of two anionic groups. An ab initio quantum chemical and molecular mechanics study of dimethyl phosphate and formate bridged by calcium and magnesium ions, J. Biomol. Struct. Dyn. 6(6) (1989) 1077–1091. [PubMed: 2818858]

[53]. Wang DW, et al., Bridging interactions and selective nanoparticle aggregation mediated by monovalent cations, Acs Nano 5(1) (2011) 530–536. [PubMed: 21182267]

[54]. Oncsik T, et al., Specific ion effects on particle aggregation induced by monovalent salts within the hofmeister series, Langmuir 31(13) (2015) 3799–3807. [PubMed: 25777544]

[55]. Zyuzin MV, et al., Influence of temperature on the colloidal stability of polymer-coated Gold nanoparticles in cell culture media, Small 12(13) (2016) 1723–1731. [PubMed: 26835654]

[56]. Fatehah MO, Aziz HA, Stoll S, Stability of ZnO nanoparticles in solution. Influence of pH, dissolution, aggregation and disaggregation effects, J. Colloid Sci. Biotechnol. 3(1) (2014) 75–84.

[57]. Schuster BS, et al., Particle tracking in drug and gene delivery research: State-of-the-art applications and methods, Adv. Drug Deliv. Rev. 91 (2015) 70–91. [PubMed: 25858664]

[58]. Gillies GT, et al., Positive pressure infusion of therapeutic agents into brain tissues: mathematical and experimental simulations, Technol Health Care 13(4) (2005) 235–243. [PubMed: 16055972]

[59]. Yang HT, Balhoff MT, Pore-network modeling of particle retention in porous media, AlChE J. 63 (7) (2017) 3118–3131.

[60]. Yoon JS, Germaine JT, Culligan PJ, Visualization of particle behavior within a porous medium: mechanisms for particle filtration and retardation during down-ward transport, Water Resour. Res. 42(6) (2006).

[61]. Pernodet N, Maaloum M, Tinland B, Pore size of agarose gels by atomic force microscopy, Electrophoresis 18(1) (1997) 55–58. [PubMed: 9059821]

[62]. Wylie RG, et al., Spatially controlled simultaneous patterning of multiple growth factors in three-dimensional hydrogels, Nat. Mater. 10(10) (2011) 799–806. [PubMed: 21874004]

[63]. DeForest CA, Anseth KS, Advances in bioactive hydrogels to probe and direct cell fate, Annu. Rev. Chem. Biomol. Eng. 3 (2012) 421–444. [PubMed: 22524507]

[64]. Zhang YS, Khademhosseini A, Advances in engineering hydrogels, Science 356(6337) (2017).

[65]. DeForest CA, Anseth KS, Photoreversible patterning of biomolecules within click-based hydrogels, Angew. Chem. Int. Ed. Engl. 51(8) (2012) 1816–1819. [PubMed: 22162285]

[66]. DeForest CA, Anseth KS, Cytocompatible click-based hydrogels with dynamically tunable properties through orthogonal photoconjugation and photocleavage reactions, Nat. Chem. 3(12) (2011) 925–931. [PubMed: 22109271]

[67]. Albanese A, Chan WC, Effect of gold nanoparticle aggregation on cell uptake and toxicity, ACS Nano 5(7) (2011) 5478–5489. [PubMed: 21692495]

[68]. Breunig M, Bauer S, Goefferich A, Polymers and nanoparticles: intelligent tools for intracellular targeting? Eur. J. Pharm. Biopharm. 68 (1) (2008) 112–128. [PubMed: 17804211]

[69]. Casey JR, Grinstein S, Orlowski J, Sensors and regulators of intracellular pH, Nat. Rev. Mol. Cell Biol. 11(1) (2010) 50–61. [PubMed: 19997129]

[70]. Brini M, et al., Neuronal calcium signaling: function and dysfunction, Cell Mol. Life Sci. 71(15) (2014) 2787–2814. [PubMed: 24442513]

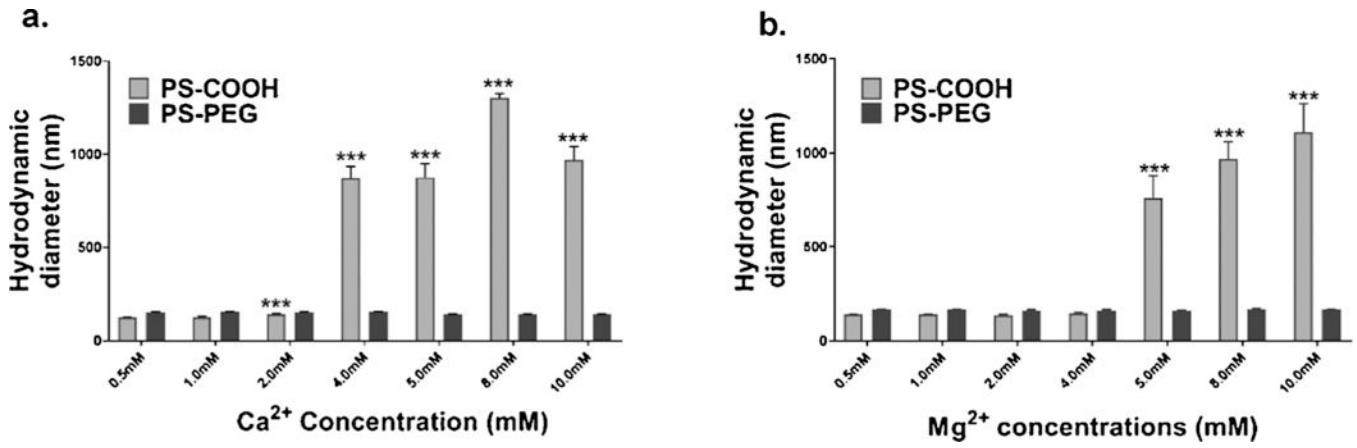

Fig. 1.

Physicochemical characterization of 100 nm PS nanoparticles in calcium solutions. (a) Hydrodynamic diameters of PS-COOH and PS-PEG nanoparticles in varying concentrations of aqueous calcium chloride solutions as measured by DLS (n = 3). (b) Hydrodynamic diameters of PS-COOH and PS-PEG nanoparticles in varying concentrations of magnesium chloride solutions as measured by DLS (n = 3). All values are reported as mean ± SEM. Significance as compared with 0 mM condition are indicated by * $p < 0.033$, ** $p < 0.002$, *** $p < 0.001$.

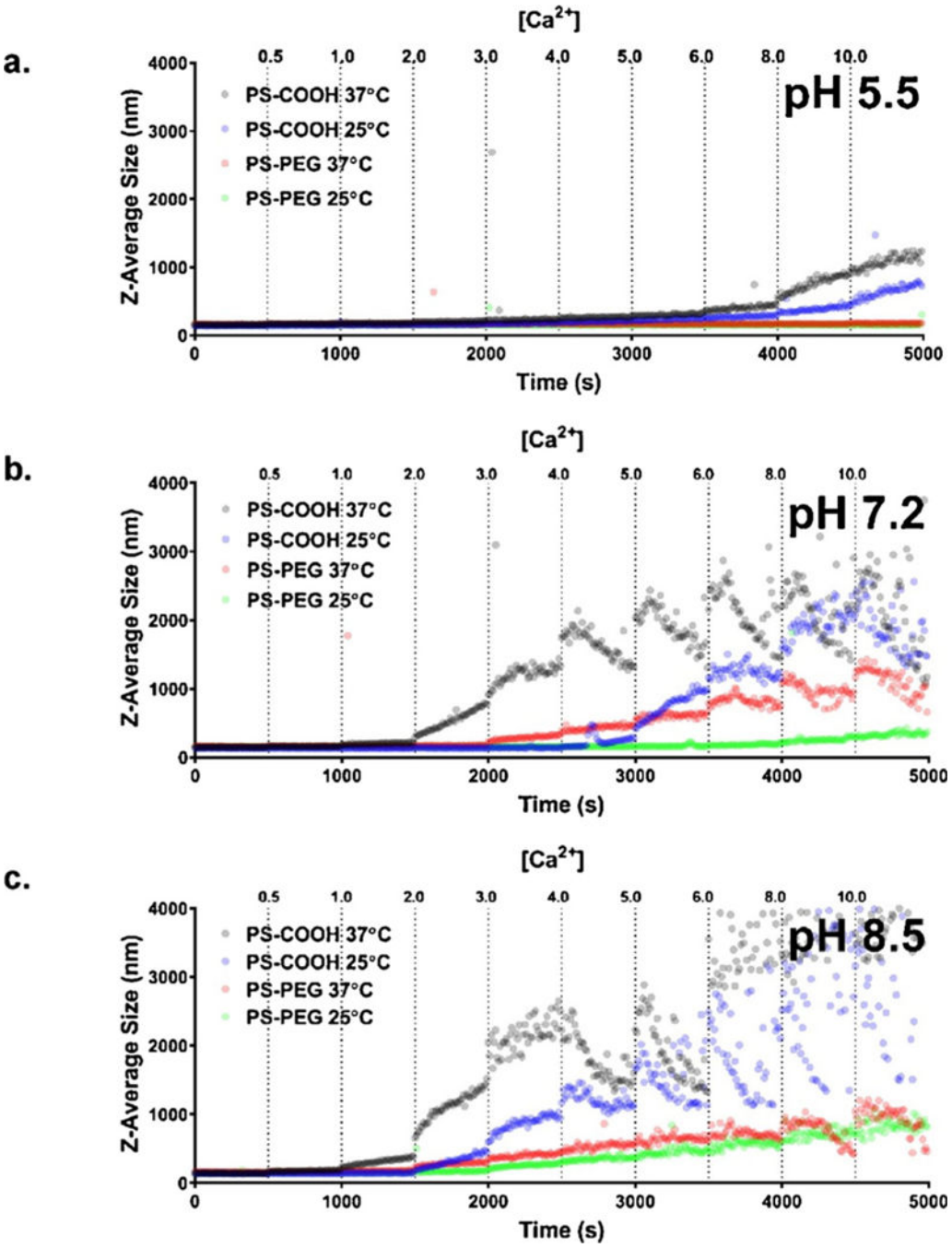

Fig. 2.

Aggregation in ACSF as a function of calcium chloride concentration. Aggregation profiles of 100 nm PS-COOH and PS-PEG nanoparticles at 25 °C and 37 °C in ACSF pH (a) 5.5, (b) 7.2, and (c) 8.5 at increasing calcium chloride concentrations from 0mM to 10 mM (n = 1).

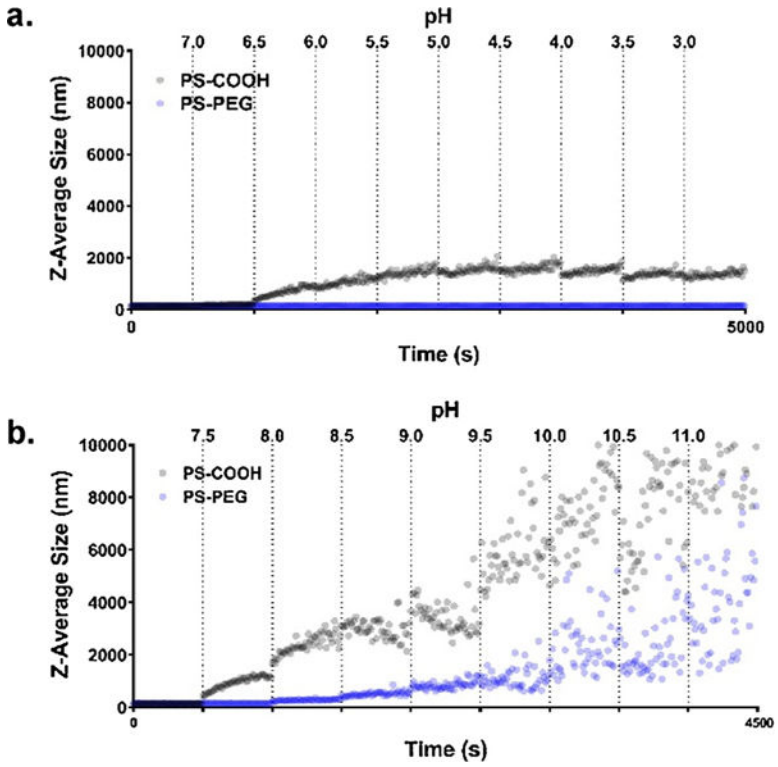

Fig. 3.

Aggregation as a function of pH. Aggregation profiles of 100 nm PS-COOH and PS-PEG nanoparticles at 25 °C and 4 mM calcium chloride in ACSF (a) at increasingly acidic conditions from pH 7.2 to pH 3.0 (n = 1) and (b) at increasingly basic conditions from pH 7.2 to pH 11.0 (n = 1).

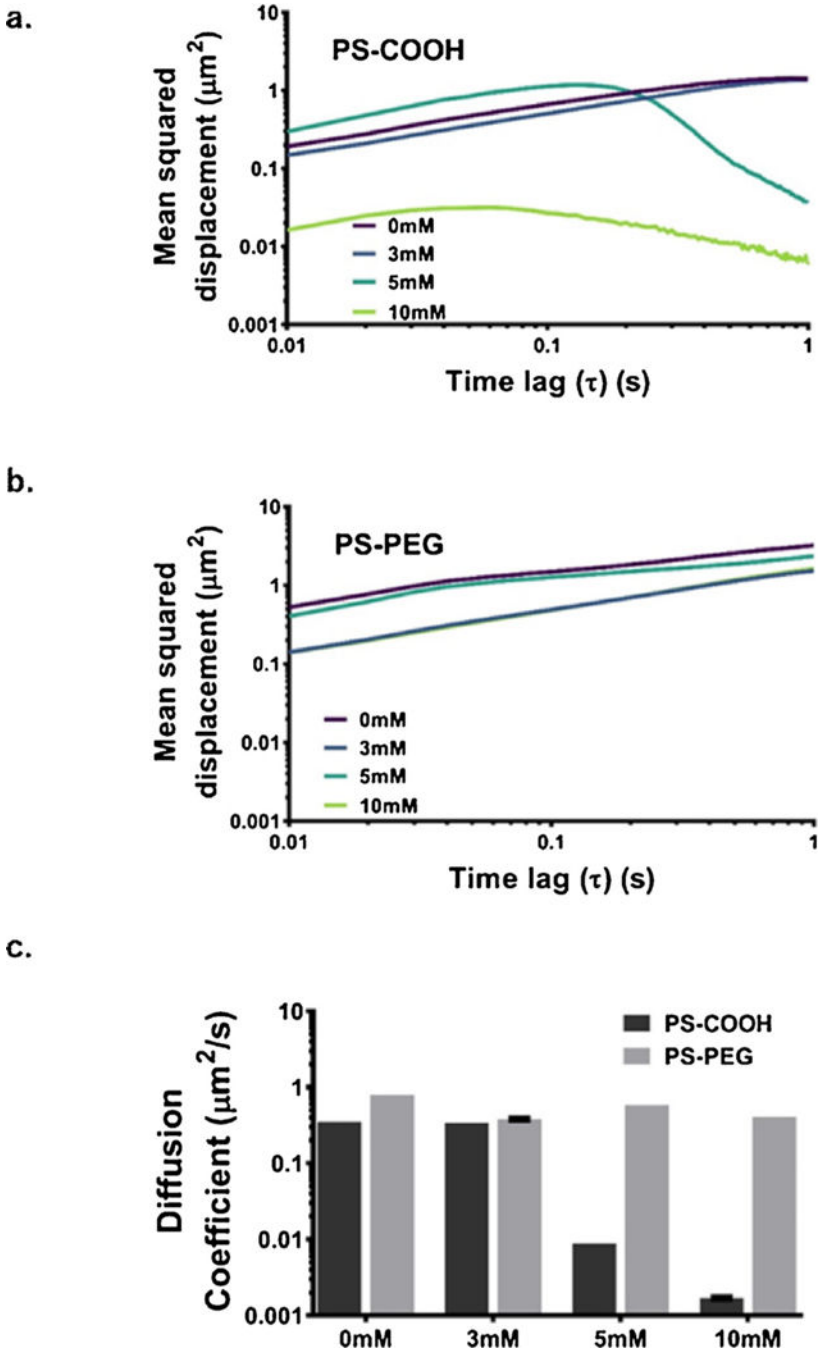

Fig. 4.

Diffusion data in agarose gels. Precision-weighted MSD profiles as a function of time lag (τ) for (a) PS-COOH nanoparticles and (b) PS-PEG nanoparticles in 0.4% in ACSF agarose gels at increasing calcium chloride concentrations (0, 3, 5, and 10 mM). Data represent the precision-weighted geometric averages over videos per well (n = 5) and wells per condition (n = 4). Error bars at τ = 0.1, 0.5, and 1 s represent 95% CIs. (c) Diffusion coefficients of PS-COOH and PS-PEG nanoparticles in agarose gels calculated at 1 s calculated as $< MSD > = 4D\tau$.

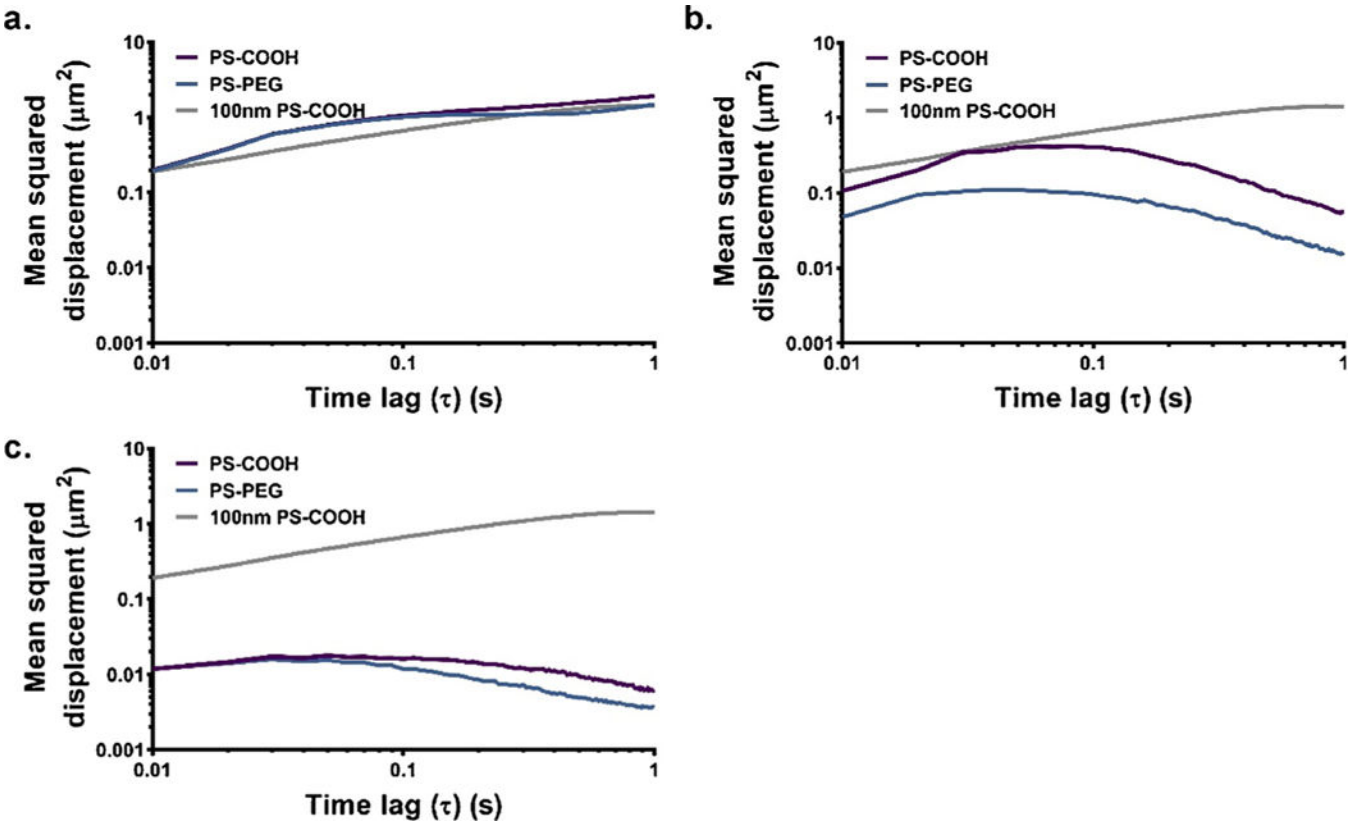

Fig. 5.

MSD profiles of PS-COOH and PS-PEG nanoparticle samples of varying average particle sizes to mimic nanoparticles in various stages of aggregation. This includes (a) equal mass fractions of 100, 200, 500, 1000, and 2000 nm PS-COOH (purple) or PS-PEG NPs (blue) in ACSF without calcium chloride, (b) equal particle concentrations of 100, 200, 500, 1000, and 2000 nm PS-COOH or PS-PEG NPs in ACSF without calcium chloride, and (c) 2000 nm PS-COOH or PS-PEG NPs in ACSF without calcium chloride. Data represent the precision-weighted geometric MSD averages over videos per well (n = 5) and wells per condition (n = 4). Error bars at τ = 0.1, 0.5, and 1 s represent 95% CIs. MSD values of 100 nm PS-COOH NPs (grey) in similar conditions is provided as a reference in all plots. (For interpretation of the references to color in this figure legend, the reader is referred to the web version of this article.)

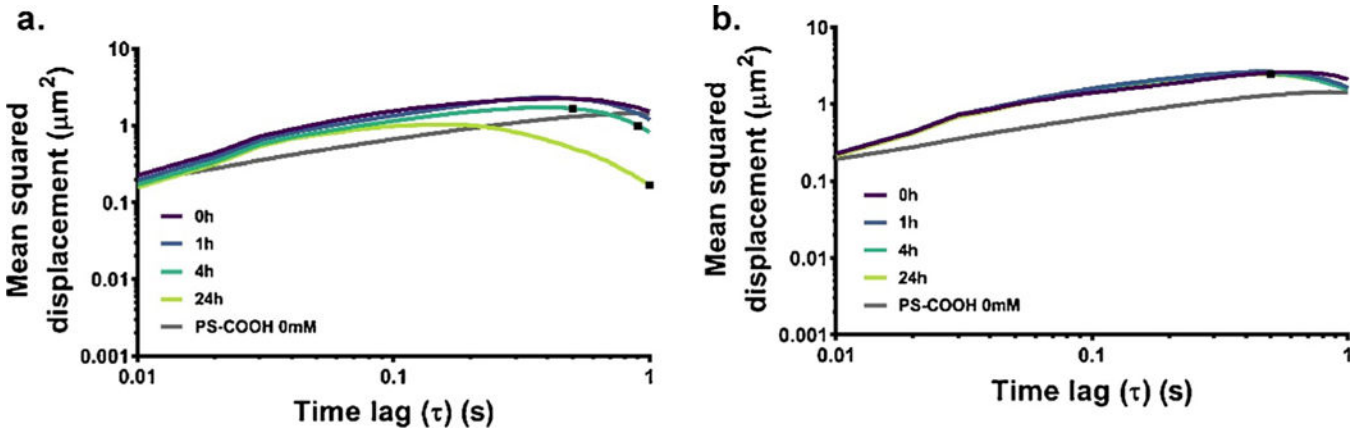

Fig. 6.

Time-dependence of diffusion in agarose gels. MSD profiles of 100 nm (a) PS-COOH and (b) PS-PEG NPs in 0.4% agarose gels constituted with ACSF 5 mM calcium chloride (aggregating conditions) at 0 (purple), 1 (blue), 4 (teal), or 24 h (lime) after gelation. Data represent the precision-weighted geometric MSD averages over videos per well (n = 5) and wells per condition (n = 4). Error bars at τ = 0.1, 0.5, and 1 s represent 95% CIs. MSD values of 100 nm PS-COOH NPs (grey) in similar conditions is provided as a reference in all plots. (For interpretation of the references to color in this figure legend, the reader is referred to the web version of this article.)

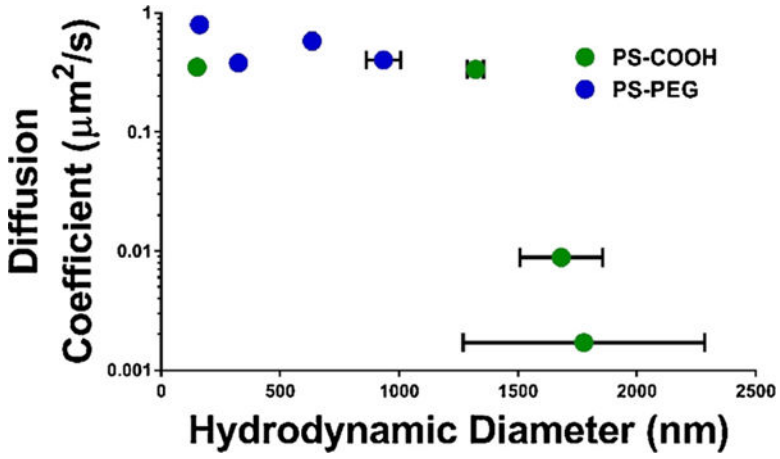

Fig. 7.

Diffusion coefficients of PS-COOH and PS-PEG nanoparticles in 0.4% agarose gels constituted with ACSF with 0/3/5/10 mM calcium chloride as a function of hydrodynamic diameter measured in ACSF with similar calcium concentrations. Error bars represent SEM.

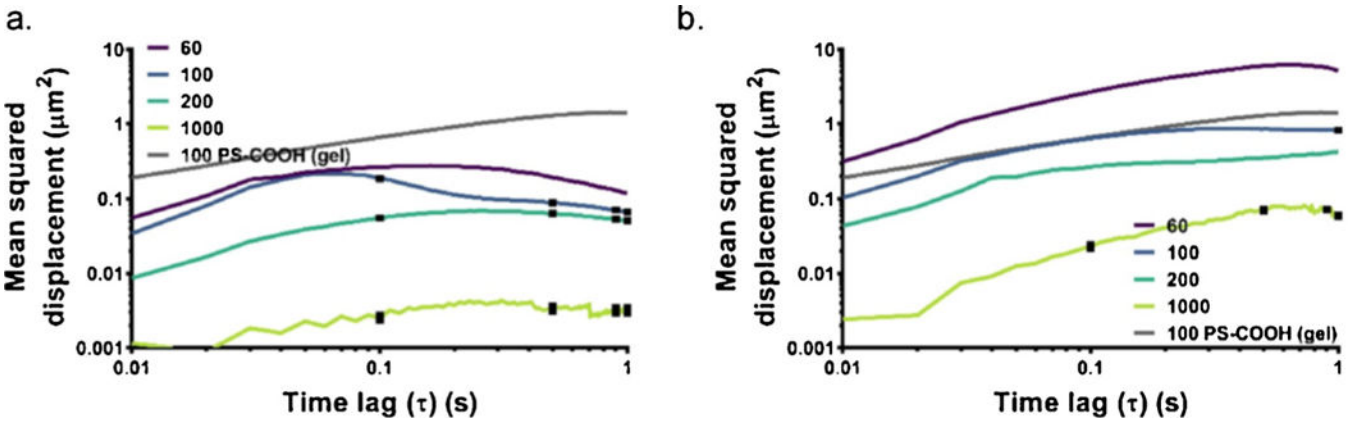

Fig. 8.

MSD profiles in cortex. Data collected using 60 (purple), 100 (blue), 200 (teal), and 1000 nm (lime) (a) PS-COOH and (b) PS-PEG NPs in the cortex region of 300μm-thick brain slices from P14 Sprague-Dawley rats. Data represent the precision-weighted geometric MSD averages over number of videos per slice (n=5) and number of slices per condition (n=3). Error bars at τ=0.1, 0.5, and 1 s represent 95% CIs. MSD values of 100 nm PSCOOH NPs (grey) in agarose gel is provided as a reference in all plots. (For interpretation of the references to color in this figure legend, the reader is referred to the web version of this article.)

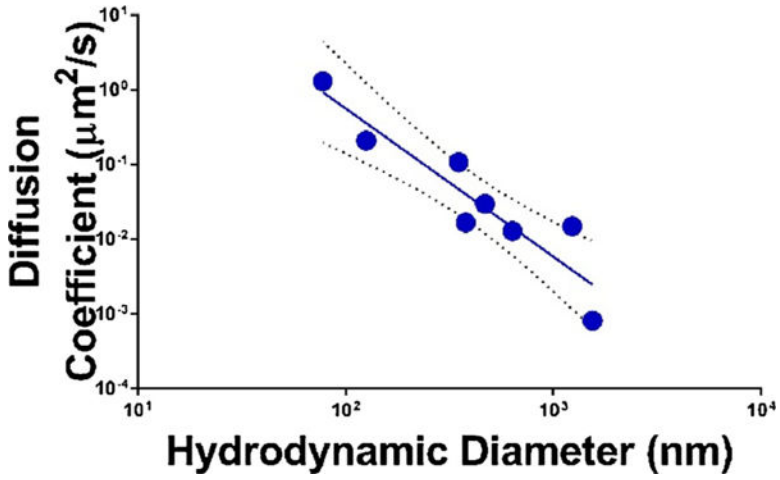

Fig. 9.

Diffusion coefficients of 60, 100, 200, and 1000 nm PS-COOH and PS-PEG NPs as measured in the cortex region of 300μm-thick brain slices from P14 Sprague-Dawley rats as a function of the hydrodynamic diameter measured in ACSF at 37 °C. The data includes a linear fit (solid line) on the log transform of both the diffusion coefficients and the hydrodynamic diameters. Error bars represent 95% confidence intervals (dashed lines) of the linear fit.

Table 1

Physicochemical characterization of PS nanoparticles including hydrodynamic diameter and ζ-potential in 10 mM NaCl at 23 °C. Data was collected *via* DLS and ZetaSizer (n = 3). All values are reported as mean ± standard error (SEM).

Particle Size (nm)	Surface Coating	Mean hydrodynamic diameter ± SEM (nm)	Mean ζ-potential ± SEM (mV)	PDI ± SEM
60	COOH	49.0 ± 2.4	− 23.3 ± 2.3	0.14 ± 0.0
60	PEG	54.3 ± 2.3	− 1.4 ± 0.5	0.20 ± 0.0
100	COOH	110.3 ± 1.6	− 68.8 ± 0.8	0.04 ± 0.0
100	PEG	127.2 ± 1.0	−3.1 ± 0.1	0.02 ± 0.0
200	COOH	216.1 ± 2.4	−56.2 ± 2.0	0.01 ± 0.0
200	PEG	237.0 ± 1.5	−7.6 ± 0.4	0.02 ± 0.0
500	COOH	416.1 ± 6.0	−48.5 ± 1.4	0.05 ± 0.0
500	PEG	545.2 ± 3.6	−4.4 ± 0.1	0.05 ± 0.0
1000	COOH	1167 ± 34	−73.8 ± 2.4	0.44 ± 0.3
1000	PEG	1019 ± 22	—3.4 ± 0.2	0.57 ± 0.3
2000	COOH	1091 ± 106	−47.6 ± 2.2	0.51 ± 0.3
2000	PEG	1271 ± 47	−4.2 ± 0.7	0.43 ± 0.4

Colloids Surf B Biointerfaces. Author manuscript; available in PMC 2019 July 30.